Lawrence Berkeley National Laboratory
LBL Publications

Title
Vacuum-Healing of Grain Boundaries in Sodium-Doped CuInSe2 Solar Cell Absorbers

Permalink
https://escholarship.org/uc/item/6tj70242

Journal
Advanced Energy Materials, 13(17)

ISSN
1614-6832

Authors
Babbe, Finn
Nicoara, Nicoleta
Guthrey, Harvey
et al.

Publication Date
2023-05-01

DOI
10.1002/aenm.202204183

WILEY-VCH

Title Vacuum-healing of grain boundaries in sodium-doped CuInSe$_2$ solar cell absorbers

Finn Babbe, Nicoleta Nicoara, Harvey Guthrey, Nathalie Valle, Omar Ramirez Sanchez, Damien Aureau, Hossam Elanzeery, Deepanjan Sharma, José Luís Virtuoso, Jean-Nicolas Audinot, Anastasiya Zelenina, Sevan Gharabeiki, Tom Wirtz, Susanne Siebentritt, Phillip J. Dale, Sascha Sadewasser, Diego Colombara*

((Optional Dedication))

Dr. F. Babbe
Chemical Sciences Division, Lawrence Berkeley National Laboratory, Berkeley, CA 94720
USA

Dr. N. Nicoara, J. L. Virtuoso, D. Sharma, Dr. S. Sadewasser
International Iberian Nanotechnology Laboratory, Braga, Av. Mestre Jose Veiga, 4715-330,
Portugal

Dr. H. Guthrey
National Renewable Energy Laboratory, Lakewood, 1617 Cole Blvd, CO 80401, USA

Dr. N. Valle, Dr. J.-N. Audinot, Dr. T. Wirtz
Luxembourg Institute of Science and Technology, Material Research & Technology
Department, Belvaux, 41 Rue du Brill, L-4422, Luxembourg

O. Ramirez Sanchez, Dr. H. Elanzeery, Dr. F. Babbe, Dr. A. Zelenina, S. Gharabeiki, Prof. S.
Siebentritt, Prof. P.J. Dale
University of Luxembourg, Physics and Materials Science Research Unit, Belvaux, 41 Rue du
Brill, L-4422, Luxembourg

Dr. D. Aureau
University of Versailles, Institut Lavoisier, Versailles, 45 Avenue des États Unis, 78000, France

Dr. H. Elanzeery, Dr. A. Zelenina
Avancis GmbH, Otto-Hahn-Ring 6, 81739 München, Germany

Dr. D. Colombara
Università degli Studi di Genova, via Dodecaneso 31, 16146 Genova, Italy
E-mail: diego.colombara@bath.edu

Alkali metal doping and grain boundaries have been at the centre of the attention within the

Cu(In,Ga)(S,Se)$_2$ photovoltaics community for years. This study provides the first experimental

evidence that the grain boundaries of sodium-doped CuInSe$_2$ thin films may undertake

1

reversible oxidation even at room temperature, whereas undoped films may not. The findings are corroborated by cathodoluminescence imaging, secondary ion mass spectrometry and Kelvin probe force microscopy on air-exposed films subsequently subject to vacuum. A thermochemical assessment identifies the likely solid-gas equilibria involved. These reactions open new research questions with respect to the beneficial role played by alkali metal dopants in chalcopyrite solar cells and may steer the community towards new breakthroughs.

$Cu(In,Ga)Se_2$ (CIGS) solar cells are the leading thin film photovoltaic technology in terms of power conversion efficiency. Yet, nearly 25 years after the seminal work by Kronik et al. on the so-called "sodium effect" [1], and despite a triple digit number of publications and patents on the topic, alkali metal doping of CIGS keeps stimulating intense debates as to the root mechanism of its efficiency boosting properties [2–8].

The classical explanation for the beneficial enhancement of p-type conductivity in CIGS by sodium extrinsic doping was to assume a replacement of (In_{Cu}) antisite donor defects by neutral (Na_{Cu}) substitutionals [9]. However, since (In_{Cu}) defects were suggested to be highly stabilized both thermodynamically and kinetically [10], the discussion on the extraordinary role played by sodium in CIGS was reopened.

The latest interpretation by Yuan et al. [2] focuses on the bulk of the CIGS grains. According to their model, the solubility of sodium as (Na_{Cu}) increases at high temperature, causing Cu to migrate out of the grains. When the samples are then cooled down, the solubility of sodium decreases, i.e. sodium is expelled from the grain interior and its excess later removed by rinsing. The end result would be an increased concentration of copper vacancies (V_{Cu}) in the CIGS grains, which would then explain the increased p-type doping of CIGS films exposed to sodium.

Once segregating at grain boundaries, sodium was also proposed to passivate defects there [11]. However, as per the grain interior case, it is unclear how sodium could play a direct role from an electronic viewpoint. The pioneering chemical passivation mechanism proposed by

Kronik et al. in 1998 [1] suggests that sodium catalyses the oxygenation of selenium vacancies. Selenium vacancies were proposed to otherwise form amphoteric complexes with copper vacancies in copper-poor surfaces and grain boundaries, which was recently confirmed to cause device performance losses [12]. By easing the formation of O_{Se} substitutionals, sodium helps neutralizing the amphoteric defect complex, thus passivating grain boundaries.

The present research shows that sodium located at the grain boundaries of $CuInSe_2$ (CIS) also minimizes the detrimental oxidation of indium and copper acting as sacrificial getters of molecular oxygen. This gettering reaction is a reversible solid-gas equilibrium, as revealed by secondary ion mass spectrometry (SIMS) depth profiling and nano-imaging on specimens deliberately exposed to air and subsequently subjected to ultra-high vacuum (UHV). A recently developed SIMS imaging technique on a helium ion microscope (HIM) [13,14] reveals preferential oxidation of grain boundaries and edges with a sub 20 nm resolution. The chemical composition of the surface and the reversibility of the oxygen chemisorption are analysed by X-ray photoelectron spectroscopy (XPS), and the consequences of the equilibrium reaction for the compound's optoelectronic properties are investigated by cathodoluminescence (CL) spectrum imaging and Kelvin probe force microscopy (KPFM).

Figure 1 provides high spatial resolution information on the elemental distribution within the Na-doped air-exposed film acquired by HIM-SIMS. The ^{16}O (red, R) and ^{80}Se (green, G) SIMS maps enable the superposition with either ^{23}Na or ^{115}In signal (both blue, B), leading to the corresponding RGB combinations. These show that the grain boundaries display comparatively higher intensities for both Na and In, consistent with the known segregation of Na and $CuIn_3Se_5$ (ordered defect compound) at grain boundaries [15,16]. Some (but not all) grain boundary regions also display high O and Se SIMS signals, thus appearing white in the superposed images. The coexistence of O, Se, Na and In in some regions is a potential sign of partial oxidation of the air-exposed CIS film. The correlation between ^{16}O and ^{23}Na ions yields a map (c) with magenta areas that match well with the spatial distribution of the ($^{16}O^{23}Na$)

atomic clusters removed by the primary ion bombardment and detected independently (d). The O-Na correlation suggests that O is not simply physisorbed, but chemically bound (at least to Na). The higher ^{16}O signal at the grain edges is consistent with preferential reaction due to a gas phase diffusion-limitation.

Surface oxidation also occurs on undoped CIS. Figure 1e shows the images of the undoped and Na-doped films exposed to air for 2h, with Fig.1f-g showing the corresponding ^{16}O ion SIMS images. The Na-doped film displays a higher ^{16}O SIMS signal than the undoped film at the bare surface. Sputter-rastering of the films surface with a 20 keV Ne$^+$ beam reduces substantially the overall ^{16}O SIMS signal. Crucially, the sputtering reveals that the Na-doped film contains submicrometer sized zones with high O content, clearly absent in the undoped film. These submicrometer-sized zones are named aggregates thereafter.
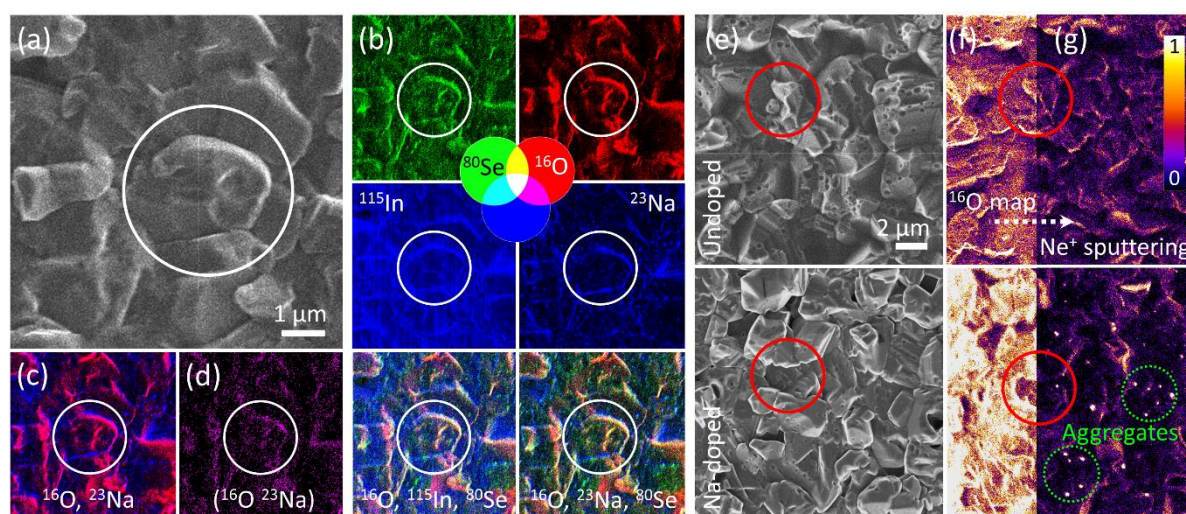
Figure 1 (a) He induced secondary electron micrograph of the Na-doped CIS film after 2h of air-exposure. **(b)** Corresponding correlative SIMS elemental distributions of ^{80}Se (green), ^{16}O (red), ^{23}Na and ^{115}In (blue), and corresponding superpositions. **(c)** Corresponding overlay of the O (red, m/z = 15.995 amu) and Na (blue, m/z = 22.990 amu) SIMS images. **(d)** Corresponding distribution of the ($^{16}O^{23}Na$) atomic cluster measured at mass m/z = 38.985 amu. **(e)** He induced secondary electron micrographs showing the morphology of undoped (top) and Na-doped (bottom) CIS films after 2h of air exposure and **(f-g)** corresponding ^{16}O SIMS images of the bare oxidised surface (f) and of the identical surface after material removal by Ne$^+$ sputtering (g). The same normalised intensity scale applies to SIMS images in (f) and (g). Solid circles are guides to the eye. Dashed green circles highlight the presence of aggregates with high O content in the Na-doped films. Note that the blisters in (e) are caused by He gas accumulation [17].

In order to add in-depth compositional information to the bidimensional surface imaging of Fig. 1g, **Figure 2** shows a series of ^{16}O Nano-SIMS images acquired through the depth of the oxidized Na-doped film. ^{16}O Nano-SIMS images at three different depths are selected to highlight one of the following: grain interiors (GI, Fig. 2b), aggregates (Fig. 2c) and grain boundaries (GB, Fig. 2d). The ensemble of locations and corresponding ^{16}O (red), (^{16}O^{23}Na) (blue) and ^{63}Cu (green) depth profiles are shown in Fig. 2e and Fig. 2f, respectively. With the visual aid of the marking circles, it is clear that the aggregates do not necessarily occur preferentially at grain boundaries, but seem to grow (or have segregated) in their vicinity. SIMS provides semi-quantitative compositional information in the absence of calibrated standards. The aggregates yield the highest ^{16}O, (^{16}O^{23}Na) and ^{63}Cu SIMS signals, followed by GB and GI. Despite a lower sensitivity for the (^{16}O^{23}Na) atomic cluster, it is clear that the (^{16}O^{23}Na) signal correlates spatially with ^{16}O through the depth of the film. The Na-O correlation is consistent with earlier evidence in CIGS and Mo [18–21], confirmed recently in the kesterite system [22]. The ^{63}Cu depth profiles also correlate with ^{16}O and the (^{16}O^{23}Na), especially in the aggregates, where oxidation has occurred to the largest extent. Cu ions are known to behave similarly to alkali metal ions in a number of phases. Therefore, it is not surprising that a Cu-containing residual of CIS decomposition coexists with Na and O.
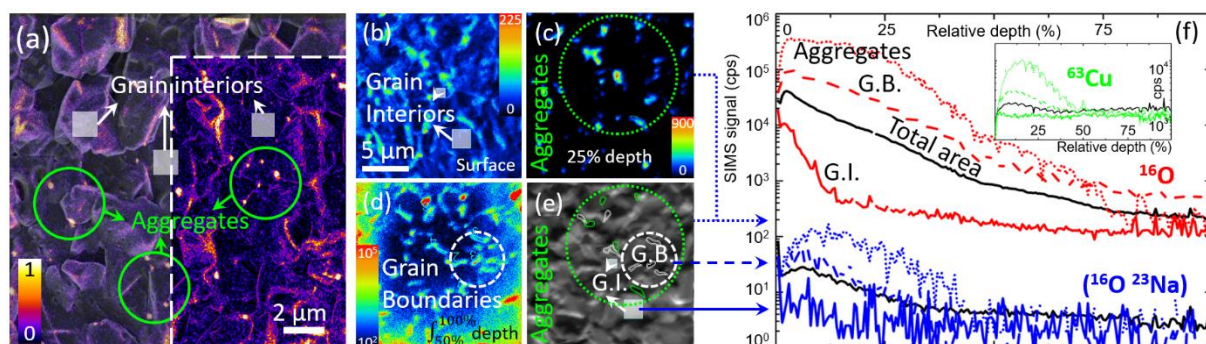

Figure 2 (a) Laplacian pyramid fusion [23] (dashed smaller portion) and overlay (remaining portion) of the Ne$^+$-sputtered ^{16}O SIMS image and He induced secondary electron micrographs (shown in Fig. 1e-g) corresponding to the Na-doped CIS film air-exposed for 2h, enabling the identification of both aggregates and grain interiors. **(b-d)** ^{16}O Nano-SIMS images of the same sample (with a different instrument at a different location) obtained at the surface (b), at 25 % relative depth (c), and integrated between 50 % and 100 % relative depth (d). **(e)** Secondary electron image corresponding to the same area in (b-d) with highlighted grain interior (GI),

grain boundaries (GB) and aggregates sites of interest. **(f)** Cumulated area-normalised ^{16}O (red) and ($^{16}O^{23}Na$) (blue) SIMS depth profiles reconstructed from the sites of interest highlighted in (b-e). The black solid lines correspond to the total SIMS signals for the whole imaged area. The ^{63}Cu depth profiles (green) are shown in the inset for clarity.

The spatial correlation between the ^{16}O and the ($^{16}O^{23}Na$) atomic cluster signals shown in

Fig. 3a corresponds to > 90 % overlap (*cf.* Fig. S1), suggesting further that O and Na are likely

bound together. Exposure to vacuum reduces substantially the ^{16}O signal, but the distribution

of the ($^{16}O^{23}Na$) atomic cluster signal appears unchanged. This suggests that the aggregates lose

O during the vacuum treatment but still contain enough O to be detected via the ($^{16}O^{23}Na$)

atomic cluster. In order to assess the reversible nature of the oxygen loss, Figure 3b shows the

^{16}O SIMS depth distribution averaged over an area of *ca.* 3000 µm^2 of a pristine Na-doped film

(solid line) and after 2 h of air exposure at room temperature (dashed line). O penetrates the

film to a depth of at least 0.6 µm, as the ^{16}O SIMS signal increases by *ca.* one order of magnitude.

The film is then left in UHV for 10 h and 14 h and the O content decreases back almost to the

original level (dotted lines).

Figure 3c shows the O1s, Se3d and Cu2p3 XPS spectra of the undoped and Na-doped films

after 2h of air exposure and subsequent 16h of vacuum (averaged over an area *ca.* 10 times as

large as that of the SIMS depth profiles shown in Fig. 3b). Peak assignment is consistent with

the extensive study by Loubat et al. [21]. The O concentration of the Na-doped film is higher

compared to the undoped film after air exposure, consistent with Fig. 1. The Se3d signal shows

two distinct contributions. The doublet at low binding energies is compatible with both CuInSe$_2$

and elemental Se, while the peak at 59 eV binding energy is a known signature of Se-O bonds.

Exposure to vacuum leads to a decrease of the O1s and Se-O peaks, while the Cu2p3 and

the lower energy Se3d peaks increase. Both effects are reversible and consistent with a

deoxygenation of the CIS surface (In3d signal also increases with vacuum, *cf.* Fig. S2). Whereas

most of the O1s signal may come from physisorbed oxygen, the higher level in the Na-doped

film and the Se3d peak near 59 eV are clear signs of chemisorption.

6
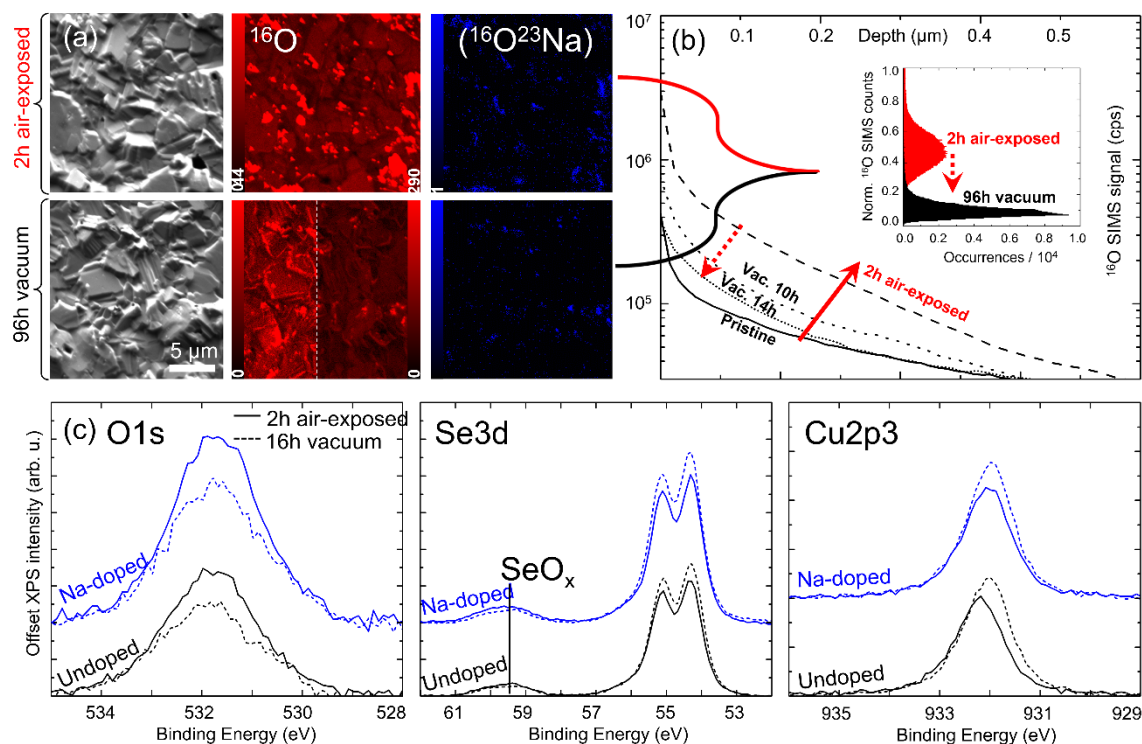
Figure 3 (a) Morphology, ^{16}O and ($^{16}O^{23}Na$) atomic cluster Nano-SIMS images of a Na-doped CIS film before and after 96 h of UHV. **(b)** Inset: pixel-by-pixel histogram distribution of normalised ^{16}O counts from the SIMS maps shown in (a) before (red) and after vacuum (black). Main graph: high resolution ^{16}O SIMS depth profiles (obtained with the CAMECA SC-Ultra depth profiling instrument) of the film in its pristine state (solid), after air exposure (dashed) and after different durations of UHV (dotted lines). **(c)** Offset O1s, Se3d and Cu2p3 XPS spectra of undoped and Na-doped CIS films after 2h of air exposure (solid lines) and subsequent 16h of vacuum (dashed lines).

In order to investigate the effect of deoxygenation on the optoelectronic properties of the films over a similar length scale to the imaging and SIMS measurements, CL spectrum imaging is performed on both undoped and Na-doped films after oxidation in air and subsequent exposure to vacuum. **Figure 4** shows the 300 K CL analysis of the films at identical locations before (left side of each image) and after (right side of each image) being subject to the SEM chamber vacuum for 75 h. For both films before vacuum, the CL intensity (Fig. 4a) largely depends on surface topography. GB regions exhibit weaker overall CL emission than GI, which is typically observed [24,25] also on polished samples [26]. Even within GI regions there are large variations seemingly caused by grain roughness and extended defects. The peak energy of the emitted

photons (Fig. 4b) reflects only weakly the grain surface topography, but GB regions display lower peak energies, due to a higher level of compensation [27,28]. Exposure to vacuum (right side of each image) induces meaningless changes to peak photon distribution and a very small decrease of the emission intensity (*cf.* Supporting Information).

The low energy side of the CL spectra is fitted with a gaussian function aimed at extracting gamma, which is a measure of the magnitude of potential fluctuations (*cf.* Supporting Information. [29]). A high gamma represents broader emission peaks, implying a higher degree of potential fluctuations. Gamma is obtained for every pixel of the map, yielding the corresponding gamma maps (c). These maps clearly reveal a higher gamma mode associated with GB regions. In the Na-doped film, the effect is so pronounced that it results in a clear bimodal gamma distribution (d). Here, the majority of pixels (mainly away from grain boundaries) display a gamma parameter below 0.1 eV, whereas a second mode around 0.15 eV appears that is correlated with grain boundaries. Exposure of the undoped film to vacuum in the SEM chamber for 75 h does not alter the gamma distribution appreciably. However, the effect in the Na-doped film is exceptional, as the higher gamma mode disappears almost completely. The effect is confirmed also for areas not previously subject to CL (*cf.* Fig. S4),
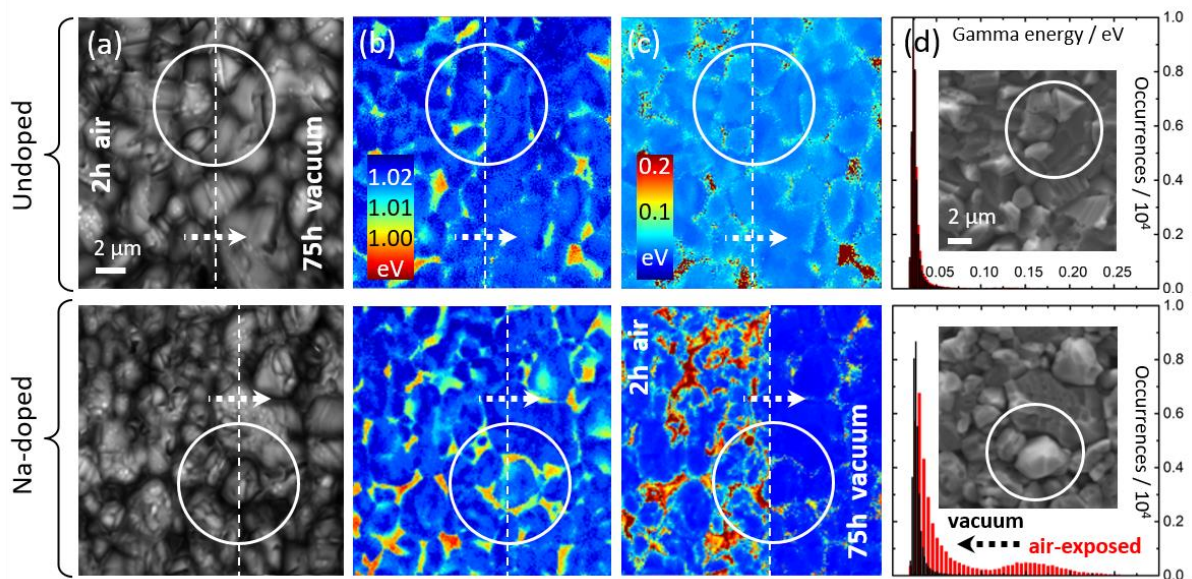

suggesting that exposure to vacuum has a healing effect on GB.

Figure 4 CL analysis at 300 K of the undoped and Na-doped CIS films after 2 h of air-exposure (left side of each image) and after 75 h of vacuum in the SEM chamber acquired at identical locations (right side of each image). **(a)** CL intensity maps. **(b)** Maps of the photon energy corresponding to the CL spectral peak of intensity (same scale applies). **(c)** Gamma parameter maps extracted by fitting the low energy side of the CL spectra at each pixel (same scale applies). **(d)** Histograms of the gamma parameter distributions. Inset: corresponding SEM micrographs of the site of interest, where the white circles indicate the same areas as in (a-c).

CL analysis is also performed at 10 K (**Figure 5a**), with the aim of gaining insights on the luminescent electronic transitions. As for the 300 K measurements, the 10 K CL yield depends on the film topography (independent of roughness, *cf.* Fig. 5b), being lower at GB compared to GI, but the overall intensity *increases* considerably after vacuum. Fig. 5c shows typical CL spectra of the air-exposed films before and after 75 h of vacuum. Three spectral features are clearly seen, attributed to the excitonic transition (EX: 1.03 eV) and donor-acceptor pair transitions (DA1: 0.99 eV and DA2: 0.97 eV) [30]. These three emission ranges are labelled in RGB format and the corresponding maps (d) indicate their dominant spatial distribution.

The accelerating voltage for the 10 K CL analysis is one third of that employed for the 300 K analysis. Therefore, charge carrier generation occurs closer to the film surface, making the results in Fig. 5d more sensitive to surface chemical effects (*cf.* Fig. S4 [31]). Exposure to vacuum clearly decreases the relative intensity of DA1 and DA2 peaks with respect to EX in the Na-doped film, while the undoped film mostly shows an overall increase of CL yield. Furthermore, there is a noticeable change in the distribution of the DA1 peak after the vacuum exposure in the Na-doped film. Prior to exposure, grain interiors are dominated by DA1 emission, whereas EX emission takes over after the exposure, with DA1 emission occurring primarily at grain boundaries. The DA2 seems unaffected by the vacuum exposure. Interestingly, the distribution of DA1, DA2, and EX emission in the undoped sample seems unaffected by the vacuum treatment.
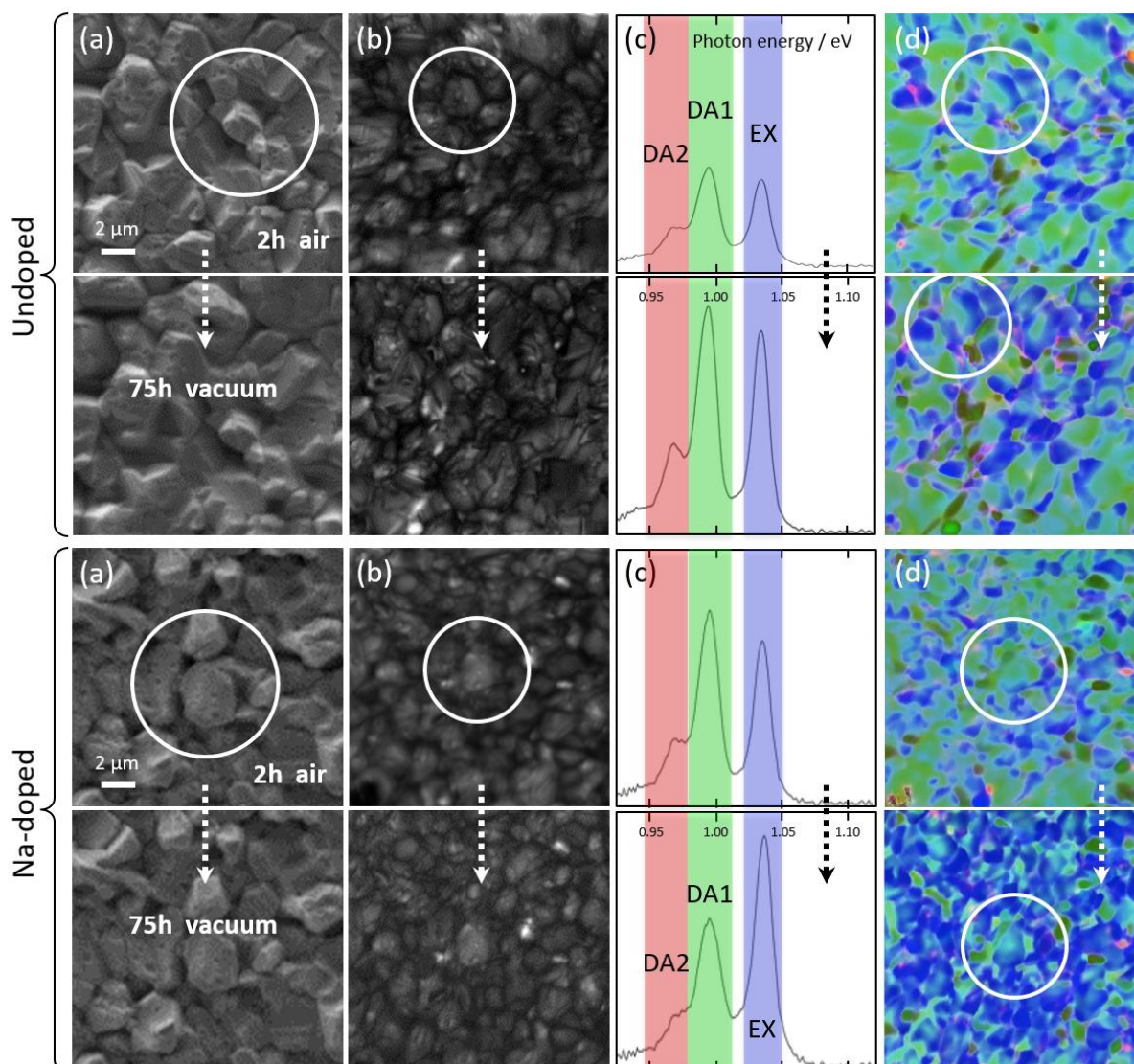
Figure 5 (a) SEM micrograph of the undoped and Na-doped CIS films analysed by CL at 10 K at identical locations after 2 h of air-exposure (top) and after 75 h of vacuum in the SEM chamber (bottom). **(b)** Corresponding CL intensity maps. **(c)** CL spectra of the films averaged over the entire analyzed areas featuring three distinct emissions labelled in RGB format (same normalized intensity applies for each sample before and after vacuum). **(d)** Corresponding RGB maps revealing the spatial distribution of the three emission ranges. The white circles are a guide to the eye for identification of the identical locations within each sample type, thus accounting for slight unintentional lateral shifts.

Comparing CL and compositional inhomogeneities can help to inspect further the correlation between surface chemistry and optoelectronic properties. **Figure 6** reports the 10 K CL map (*cf.* Fig. 5d) and SIMS compositional distribution (*cf.* Fig. 1b) of the Na-doped film at the same magnification (note that these analyses were not performed simultaneously, but comparing all the different methods side-by-side should bring added value).
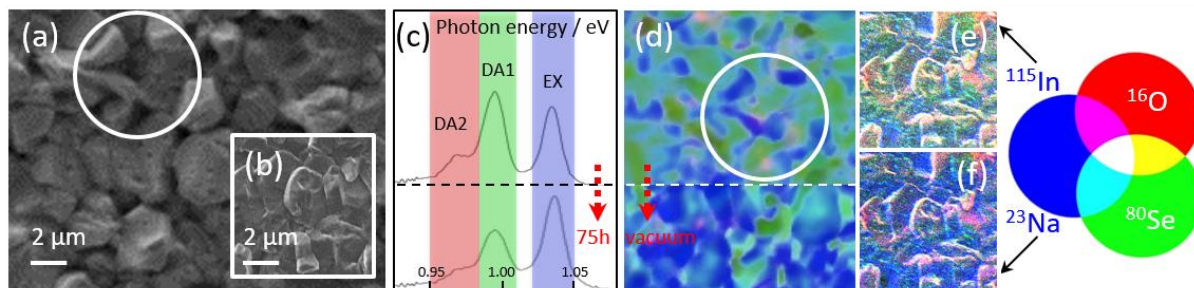
Figure 6 Ensemble of independent analyses displayed at the same magnification for discussion purposes. **(a)** SEM and **(b)** He induced secondary electron micrographs of the Na-doped CIS film exposed to air for 2 h. **(c)** 10 K CL spectrum of the film with labelling of the DA2 (red), DA1 (green) and excitonic (blue) transitions. **(d)** Correspondingly colored CL emission map at 10 K. **(e-f)** SIMS imaging of (b) with overlaid ^{16}O (red), ^{80}Se (green) and either ^{115}In (e) or ^{23}Na (f) (blue) signals.

It is clear that the length scale and visual appearance of the features in Fig. 6d-f are very similar. Exposure to vacuum appears to decrease the extent of DA pair transition in favour of the excitonic emission (Fig. 6c-d). The removal of oxygen from the Na-doped films occurs hundreds of nm below the surface, as revealed by the SIMS depth profiling (Fig. 3c) and is mostly associated to grain boundaries (*cf.* Fig. 2f). Therefore, the reduced extent of DA1 and DA2 after vacuum is directly or indirectly associated with the oxygen removal. This fact, together with the evidence of gamma reduction after vacuum (Fig. 4d), suggests that the oxygen removal from CIS surfaces and grain boundaries is beneficial, correlates with the presence of Na and is eased by Na.

The vacuum-induced CL effects are tentatively assigned to desorption of physisorbed and chemisorbed oxygen in the undoped and Na-doped films, respectively. Considering the topographical correlation between Cu, Na and O in the Na-doped film (*cf.* Fig. 2f), the oxygen removal and concurrent drop of DA1 and DA2 signals suggest a chemical reversibility of the CIS decomposition. In such a hypothetic scenario, the outgrown Cu-O phase is stripped of its oxygen and results in Cu redistribution (given its high mobility [32]), which lowers the concentration of In_{Cu} defects that are likely involved as shallow donors in both DA1 and DA2 transitions [30,33].

11

Figure 7 shows the KPFM analysis of Na-doped and undoped CIS films. The analysis includes several independent grain boundaries, across which contact potential difference (CPD) line profiles were extracted from images acquired periodically over a timeframe of > 20 h under UHV. The Na-doped film shows a progressive drop of CPD signal overtime, while being held in vacuum (Fig. 7b-c). The CPD drop is generalised, but is manifest at grain boundary regions, as shown in Fig. 7g where the CPD signal is extracted *along* the grain boundary only. Conversely, the undoped film reveals almost no change in the CPD profiles *across* the grain boundary (Fig. 7e-f), or *along* the grain boundary (Fig. 7g) and a narrower distribution of CPD over the analysed surface area (inset). By combining this information with the other experimental techniques, it is possible to state that the variation with time of the CPD signal observed for the Na-doped film is compatible with vacuum-induced charge redistribution at the film surface, and especially along the grain boundaries.
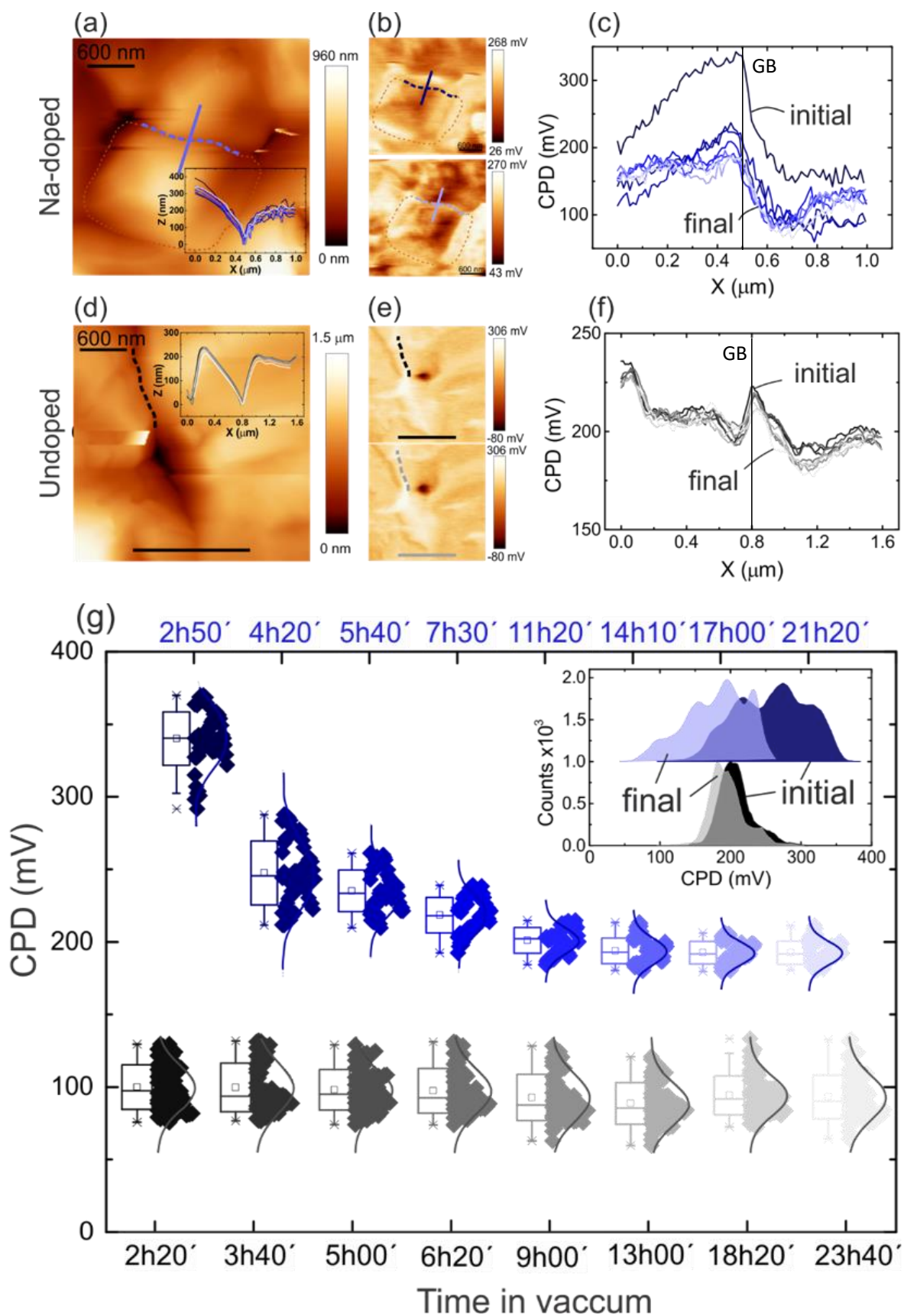
Figure 7 Topography image of the Na-doped (a) and undoped (d) air-exposed CIS films. Corresponding contact potential difference (CPD) maps (b,e) at the beginning (top) and end of acquisition (bottom). The CPD line scans *across* the grain boundaries indicated by the solid lines in (b) and (e) are shown in (c) and (f), respectively for various exposure times under UHV

13

(dark to light). (g) Distribution of CPD values *along* the grain boundaries indicated by the dashed lines in (b) and (e) as a function of exposure time under UHV. Inset: overall CPD distributions extracted from the initial (dark) and final (light) image acquisitions of the Na-doped (top) and undoped (bottom) CIS films.

In order to account for the improvements of early CIS devices upon post-fabrication air annealing, Cahen and Noufi proposed in 1991 a model involving the passivation of (V_{Se}) donors by oxygen via formation of (O_{Se}) substitutional defects [34]. It was argued that the reduction of recombination losses was directly linked to the oxygenation of selenium vacancies. Their model was later expanded by Kronik et al. when it occurred that the presence of sodium in the CIGS film diffusing from the soda lime glass (SLG) substrate made the air annealing step unnecessary [1]. A catalytic mechanism was invoked, consistent with older literature on carbon soot oxidation [35], for which the sodium-containing segregations at the CIGS surface and grain boundaries induce a polarization of the molecular oxygen bond (physisorbed on the CIGS surface *e.g.* due to air exposure), easing its dissociation into atomic oxygen and subsequent capture by V_{Se}. The result was the known increased p-type doping and reduced charge carrier recombination, leading to higher open circuit voltages [36].

Unlike early CIS devices, modern absorbers contain low initial concentrations of selenium vacancies due to the improved deposition processes. Yet, it was shown that the chemical instability of the CIS surface against oxygen causes the spontaneous formation of selenium vacancies even at room temperature, especially on CIS samples grown under Cu excess [12]. As a result, whereas a short exposure to air may be beneficial, extended air annealing of bare CIGS films is *detrimental* for absorber/buffer interfaces, as shown by Hölscher et al. [37]. Mönig et al. have shown that 280 °C annealing under UHV lead to homogeneous current imaging tunneling spectroscopy maps on bare CIS films, while the same maps acquired on films subsequently subject to air annealing display granular inhomogeneities. They concluded that thermal annealing under UHV enables to passivate CIS surface defects and increases significantly the surface band bending leading to a prospective increase of open circuit voltage [38]. In this sense,

the success of alkali metal doping seems at odd with Shin et al., who clearly showed that Na and K *promote* oxygen chemisorption into bare CIGS films [39].

These seeming contradictions are reconciled by the present study. The phenomenon observed by Mönig et al. [38] may relate to the vacuum-induced deoxidation of the CIS surface, demonstrated here at room temperature. Air exposure of bare CIS leads to the formation of mostly indium oxides – according to experimental observation [40] – but also copper oxides, according to thermochemical equations. In this study air exposure of CIS in the absence of sodium leads to lower luminescence yields and higher overall electrostatic potential fluctuations. If Na is present in the films, oxygen incorporation may be enhanced, in accordance to Shin et al. [39]. However, CIS decomposition into In and Cu oxides may be curbed thanks to the preferential formation of Na-O phases segregating into aggregates (*cf.* Fig. 2), leading to high electrostatic potential fluctuations at the grain boundaries. These phases appear to be amenable to de-oxidation upon exposure of the films to vacuum, healing the gamma parameter at grain boundaries, as revealed by CL (*cf.* Fig. 4c). The reversible nature of these equilibria is consistent with thermochemical equations shown in Figure 8a-b and with the phenomenological
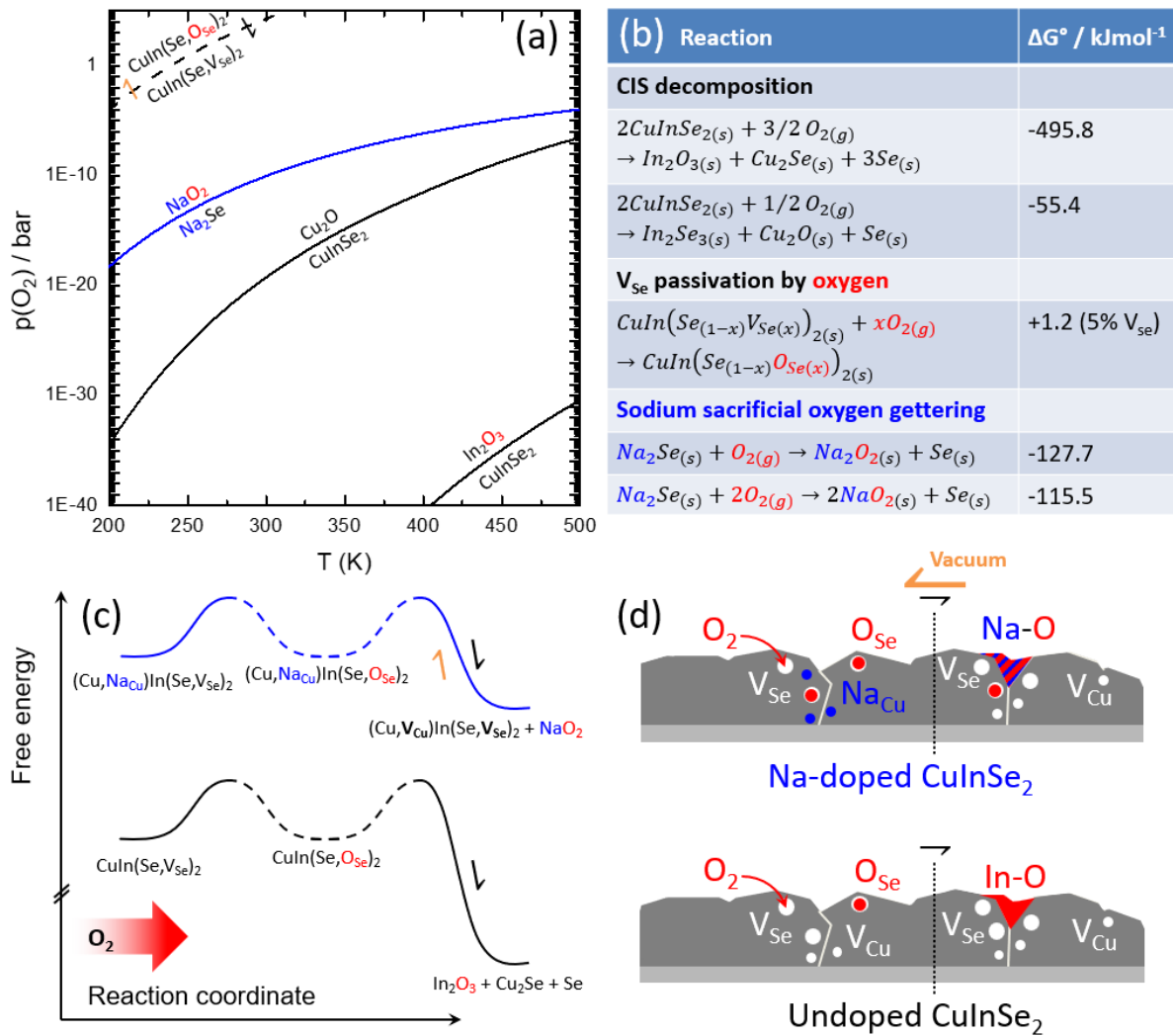
WILEY-VCH

Figure 8 (a) Temperature-Pressure(O_2) diagrams of chemical equilibria involving CIS decompositions (solid black curves) and O-uptake/release by defected CIS (black dashed), and relevant sodium (blue) phases. **(b)** Corresponding standard Gibbs free energies calculated from [41,33,42,43]. **(c)** Tentative energy diagram inspired by [12,34] and **(d)** sketch acknowledging the (ir)reversibility of grain boundary oxidation in the Na-doped (undoped) CIS film, including its consequences on point defect passivation/formation.

Previous findings indicate that oxygen initially passivates V_{Se} at the CIS surface, exerting a beneficial action, and then induces the formation of In-O and Cu-Se, generating the V_{Cu}-V_{Se} complex [12]. Hence, the phenomenological interpretation is that once O_{Se} defects are formed, they can shuffle O to other more thermodynamically favourable locations, as supported by Sahoo et al. [42]. In the case of undoped CIS, the path leads to the irreversible growth of In-O especially at grain boundaries [12]. This is even supported by a recent study where undoped air-

exposed epitaxial CIS films subject to annealing at 200 °C under UHV reveal irreversible alteration of the work function [44]. Na doping, instead, was already suggested to catalyse In-O bond formation [1,34], but it is argued here that it may also act as a sacrificial oxygen buffer by forming Na-O phases. Now, even though the growth of Na-O phases is unlikely to prevent the detrimental formation of the divacancy complex (chemical equations in Fig. 8c), the lower free energy involved ensures that the process is reversible. Upon application of vacuum, it is then possible to revert Na and O back into the CIS phase to re-passivate the divacancy complex, which would account for the drop of gamma parameter observed in the CL map (if the complex is present in its donor configuration) and for the drop of the DA1 PL peak. The equations in Fig. 8a-b do not consider the role of moisture because its effect on the energetics of ion hydration is not trivial. Nevertheless, water is likely to play a crucial role in speeding up the sacrificial oxygen gettering, as the reaction is consistent with the observed drop of resistivity in Na-doped CIGS upon exposure to (moist) air rather than pure oxygen [45], a sign of electrical ionic conduction across grains.

This study shows that Na doping minimizes the detrimental decomposition of CIS upon exposure to air and heals oxidized grain boundaries with positive effects on the radiative recombination of the bare absorbers. It confirms the catalytic effect invoked 25 years ago by Kronik to explain the Na-*enhanced* oxygen incorporation into CIS [1] and posits that oxygen *desorption* from CIS may simply be the consequence of the catalytic effect exerted by alkali metal dopants in the opposite direction. This hypothesis unites previous studies with seemingly contradicting results. Future research will be devoted to test the hypothesis, especially on heavier alkali metal dopants [46], and to identify the link between the reversibility of oxidation and the chemical processes happening in the liquid-phase still encountered during most baseline solar cell finishing [36,47]. Likewise, the impact on device performance will have to be assessed.

Experimental Section

Sample preparation and surface treatments

The CIS absorbers were fabricated by physical vapour deposition in a molecular beam epitaxy system at 530 °C using a 1-stage co-evaporation process. The substrates employed were Mo-coated soda-lime glass (Na-doped films) that in the case of undoped films also comprised an alkali metal diffusion barrier between the glass and the Mo layer. The as-prepared CIS films grown under Cu excess were etched in a KCN 10 wt. % aqueous solution for 5 minutes in order to remove any residual Cu-Se phase that may have formed during the growth, leading to a Cu/In atomic ratio of 1.07 ± 0.05 measured by energy-dispersive X-ray spectroscopy (EDS), i.e. an essentially stoichiometric $CuInSe_2$ [12]. The films were then exposed to air and analysed either with the shortest possible delay (transfer times ca. 5 minutes) or intentionally left in air for up to 24 h under dark conditions to ensure a reproducible "oxidised" surface state. Subsequently, the films were analysed under each technique's typical vacuum environment (Table 1) as soon as allowed, and after various periodic intervals, as described in the manuscript.

Table 1 – Summary of vacuum exposure conditions, duration, and relevant figures

Technique	Vacuum	Duration	Figure
HIM-SIMS	10^{-7} mbar	18 hours	1
SIMS NanoSIMS 50	10^{-9} mbar	96 hours	3a, 3b (inset)
SIMS SC-Ultra	8×10^{-9} mbar	10 hour, 14 hours	3b
XPS	10^{-7} mbar	16 hours	3c
XPS	10^{-7} mbar	Up to 88 hours	S2
CL	10^{-7} mbar	75 hours	4, 5
KPFM	4×10^{-11} mbar	> 20 hours	7

Helium and secondary ion mass spectrometry imaging (HIM-SIMS): Helium and Neon induced Secondary Electron Microscopy and Secondary Ion Mass Spectrometry images were acquired with a Helium Ion Microscope (HIM, Zeiss, Peabody (US)) coupled with an add-on SIMS system (LIST, Luxembourg) [13,14] (*cf*. Fig. 1 also reported in Fig. 2a and Fig. 6b,e,f). In this case study, the HIM-SIMS images were acquired with a 20 keV helium beam of 0.5 pA and 20 keV neon beam of 2pA, respectively. The secondary ions were collected and detected in both polarities. The SIMS images were recorded for a matrix of 512×512 pixels and with a counting time of 3 ms/pixel. In these conditions a sub 20 nm lateral resolution is expected for SIMS analysis. The air-exposed CIS film was analysed twice at an identical location, before and after ~18 hrs under vacuum (10^{-7} mbar) in the HIM chamber and for comparison on an area not scanned initially.

Secondary Ion Mass Spectrometry (SIMS): The SIMS technique has been used in two modes: depth profiling and nano-imaging. The depth-profiling was carried out on a CAMECA SC-Ultra instrument (CAMECA, France) with a 1keV Cs^+ beam. Secondary negative ions (e.g $^{16}O^-$) were collected from an area of 60 µm in diameter center on a (200×200) µm^2 sputtered area. After 2-hour of air exposure, the Na-doped CIS film was rapidly introduced in the SC-Ultra analysis chamber and then stored in a vacuum of about 8×10^{-9} mbar for successive in-depth analyses (main graph in Fig. 3b). A CAMECA NanoSIMS 50 (CAMECA, France) was used to acquire 3D (Fig. 2b-f) and 2D (Fig. 3a) SIMS images. These images were acquired with a 16 keV Cs^+ beam of 1.5 pA for studying the distribution of $^{16}O^-$, $(^{16}O^{23}Na)^-$ atomic cluster, $^{63}Cu^-$ and $^{78}Se^-$ simultaneously in multicollection mode. The Nano-SIMS images were recorded for a matrix of 256×256 pixels and with a counting time of 10 ms/pixel. The size of images was (20×20) µm^2. The size of the beam was adjusted to 150 nm as a good compromise between the sputtering rate (reasonable acquisition time to image the whole oxidized layer) and the lateral image resolution. The analysis chamber pressure was *ca*. 1×10^{-9} mbar.

Cathodoluminescence analysis (CL): The CL analysis was performed with acceleration voltage of 15 kV (at 300 K) and 5 kV (at 10 K) and a beam current of ~1nA over a scanned area of 15×15 μm^2, 200×200 pixels. The analysis of the air-exposed CIS film was repeated at the identical location after ~75hrs in SEM chamber vacuum and for comparison on a region not scanned initially, in order to exclude measurement artefacts. The CL emission intensity images are panchromatic and formed from all emission from the samples. The pixel color in the CL emission energy maps result from segmenting the emission spectrum into various energy channels (indicated in the accompanying spectra), normalizing the intensity of each pixel, and then summing the contributions of the red, green, and blue channels to determine the RGB value of each pixel. The red/green/blue color scheme was chosen because it is easy to understand the images qualitatively in terms of lower (red) to higher (blue) energy emission.

Kelvin probe force microscopy (KPFM): KPFM experiments were performed in an ultra-high vacuum scanning probe microscope (SPM), Omicron Nanotechnology GmbH, controlled by Nanonis electronics and using a PtIr-coated cantilever (f_0=167 kHz). Amplitude modulation (AM) was used for the detection of the CPD with an *ac* bias of 400 mV at the 2nd oscillation mode of the cantilever. In our setup, the CPD is defined as CPD = $\Phi_{sample} - \Phi_{tip}$.

The samples were air-exposed for ~ 22 hours and then loaded into the pre-vacuum chamber (where a decrease from atmospheric pressure to ~ 2×10^{-8} mbar occurs within ~ 18 hours), before being transferred into the analysis chamber (with a pressure of ~ 4×10^{-11} mbar). KPFM was used to locally probe the changes in the CIS surface potential, by monitoring the spatially resolved contact potential difference (CPD) in a time-dependent study. The acquisition time of a KPFM measurement, consisting of a topographic and a CPD image is approximately 1h and 30 min. A continuous scan of an identical area of the sample with 3μm × 3μm size, was performed over ~ 23 h and 40 min for the undoped-CIS sample and over ~ 21 h and 20 min for the Na-doped CIS sample. The identification of grain boundaries is performed according to the methodology described in [48].

X-ray photoelectron spectroscopy (XPS): The XPS spectrometer used is a Thermo Scientific Nexsa X-Ray System. Data was acquired using an Al Kα_1 monochromatic X-ray excitation. The photoelectrons were collected perpendicularly to the sample surface over an elliptical spot was the major axis of 400 µm. The detection was performed in a constant analyzer energy mode (CAE), using a step of 0.1 eV and a pass energy of 20 eV. For ageing measurements, the samples remained in the analysis chamber under a pressure of about 10^{-7} mbar. The data were processed using the Thermo Electron "Avantage XPS software".

Supporting Information
Supporting Information is available from the Wiley Online Library or from the author.

Authors' contributions

D.C. designed the research and wrote the manuscript in conjunction with all co-authors. H.G. performed the cathodoluminescence analyses and provided data interpretation in conjunction with D.C. and Su.S.. N.V. first observed the experimental evidence of vacuum-induced oxygen desorption by SIMS and was in charge of the SIMS processing data with input from D.S. and D.C.. O.R.S., H.E. and F.B. coordinated specimens handling/air-exposure and fabricated the CuInSe$_2$ samples in conjunction with A.Z.. The HIM-SIMS analysis was performed by J.-N.A., who interpreted the data in conjunction with T.W., N.V., D.C. and P.J.D. The KPFM analysis was performed by N.N. and D.S. who interpreted the data in conjunction with D.C. and Sa.S.. O.R.S, J.L.V., and S.G. took over sample preparation for the revision of the study. The XPS data acquisition and interpretation was performed by D.A. and D.C..

Received: ((will be filled in by the editorial staff))
Revised: ((will be filled in by the editorial staff))
Published online: ((will be filled in by the editorial staff))

References

[1]   L. Kronik, D. Cahen, H. W. Schock, *Advanced Materials* **1998**, *10*, 31.

[2]   Z. Yuan, S. Chen, Y. Xie, J.-S. Park, H. Xiang, X.-G. Gong, S.-H. Wei, *Advanced Energy Materials* **2016**, *6*, 1601191.

[3]   A. Chirilă, P. Reinhard, F. Pianezzi, P. Bloesch, A. R. Uhl, C. Fella, L. Kranz, D. Keller, C. Gretener, H. Hagendorfer, D. Jaeger, R. Erni, S. Nishiwaki, S. Buecheler, A. N. Tiwari, *Nature Materials* **2013**, *12*, 1107.

[4]   P. Jackson, R. Wuerz, D. Hariskos, E. Lotter, W. Witte, M. Powalla, *Phys. Status Solidi RRL* **2016**, *10*, 583.

[5]   D. Colombara, F. Werner, T. Schwarz, I. C. Infante, Y. Fleming, N. Valle, C. Spindler, E. Vacchieri, G. Rey, M. Guennou, M. Bouttemy, A. Garzón Manjón, I. Peral Alonso, M. Melchiorre, B. El Adib, B. Gault, D. Raabe, P. J. Dale, S. Siebentritt, *Nature Communications* **2018**, *9*, 826.

[6]   D. Colombara, *Phys. Rev. Materials* **2019**, *3*, 054602.

[7]   B. J. Stanbery, D. Abou-Ras, A. Yamada, L. Mansfield, *J. Phys. D: Appl. Phys.* **2021**, *55*, 173001.

[8]   D. Colombara, K. Conley, M. Malitckaya, H.-P. Komsa, M. J. Puska, *J. Mater. Chem. A* **2020**, *8*, 6471.

[9]   S.-H. Wei, S. B. Zhang, A. Zunger, *Journal of Applied Physics* **1999**, *85*, 7214.

[10] L. E. Oikkonen, M. G. Ganchenkova, A. P. Seitsonen, R. M. Nieminen, *Journal of Applied Physics* **2013**, *114*, 083503.

[11] A. Laemmle, R. Wuerz, T. Schwarz, O. Cojocaru-Mirédin, P.-P. Choi, M. Powalla, *Journal of Applied Physics* **2014**, *115*, 154501.

[12] D. Colombara, H. Elanzeery, N. Nicoara, D. Sharma, M. Claro, T. Schwarz, A. Koprek, M. H. Wolter, M. Melchiorre, M. Sood, N. Valle, O. Bondarchuk, F. Babbe, C. Spindler, O. Cojocaru-Miredin, D. Raabe, P. J. Dale, S. Sadewasser, S. Siebentritt, *Nature Communications* **2020**, *11*, 3634.

[13] T. Wirtz, D. Dowsett, P. Philipp, in *Helium Ion Microscopy* (Eds.: G. Hlawacek, A. Gölzhäuser), Springer International Publishing, Cham, **2016**, pp. 297–323.

[14] D. Dowsett, T. Wirtz, *Anal. Chem.* **2017**, *89*, 8957.

[15] O. Cojocaru-Mirédin, P. Choi, R. Wuerz, D. Raabe, *Ultramicroscopy* **2011**, *111*, 552.

[16] D. Keller, S. Buecheler, P. Reinhard, F. Pianezzi, B. Bissig, R. Carron, F. Hage, Q. Ramasse, R. Erni, A. N. Tiwari, *Appl. Phys. Lett.* **2016**, *109*, 153103.

[17] F. I. Allen, P. Hosemann, M. Balooch, *Scripta Materialia* **2020**, *178*, 256.

[18] D. W. Niles, M. Al-Jassim, K. Ramanathan, *Journal of Vacuum Science & Technology A* **1999**, *17*, 291.

[19] R. V. Forest, E. Eser, B. E. McCandless, R. W. Birkmire, J. G. Chen, *AIChE Journal* **2014**, *60*, 2365.

[20] T. Hölscher, S. Förster, T. Schneider, M. Maiberg, W. Widdra, R. Scheer, *Applied Physics Letters* **2017**, *111*, 011604.

[21] A. Loubat, S. Béchu, M. Bouttemy, J. Vigneron, D. Lincot, J.-F. Guillemoles, A. Etcheberry, *Journal of Vacuum Science & Technology A* **2019**, *37*, 041201.

[22] S. Grini, K. V. Sopiha, N. Ross, X. Liu, T. S. Bjørheim, C. Platzer-Björkman, C. Persson, L. Vines, *Advanced Energy Materials* **2019**, *9*, 1900740.

[23] F. Vollnhals, J.-N. Audinot, T. Wirtz, M. Mercier-Bonin, I. Fourquaux, B. Schroeppel, U. Kraushaar, V. Lev-Ram, M. H. Ellisman, S. Eswara, *Anal. Chem.* **2017**, *89*, 10702.

[24] G. Hanna, T. Glatzel, S. Sadewasser, N. Ott, H. P. Strunk, U. Rau, J. H. Werner, *Appl. Phys. A* **2006**, *82*, 1.

[25] H. Guthrey, J. Moseley, J. Nishinaga, H. Shibata, H. Takahashi, M. Al-Jassim, *IEEE Journal of Photovoltaics* **2018**, *8*, 1833.

[26] D. Abou-Ras, M. Bär, R. Caballero, R. Gunder, C. Hages, M. D. Heinemann, C. A. Kaufmann, M. Krause, S. Levcenko, R. Mainz, J. Márquez, A. Nikolaeva, A. Redinger, N. Schäfer, S. Schorr, H. Stange, T. Unold, R. G. Wilks, *Solar Energy* **2018**, *170*, 102.

[27] U. Rau, *Phys. Rev. B* **2007**, *76*, 085303.

[28] M. J. Romero, H. Du, G. Teeter, Y. Yan, M. M. Al Jassim, *Physical Review B* **2011**, *84*, 165324.

[29] E. O. Kane, *Phys. Rev.* **1963**, *131*, 79.

[30] N. Rega, S. Siebentritt, J. Albert, S. Nishiwaki, A. Zajogin, M. Ch. Lux-Steiner, R. Kniese, M. J. Romero, *Thin Solid Films* **2005**, *480–481*, 286.

[31] D. Drouin, A. R. Couture, D. Joly, X. Tastet, V. Aimez, R. Gauvin, *Scanning* **2007**, *29*, 92.

[32] L. E. Oikkonen, M. G. Ganchenkova, A. P. Seitsonen, R. M. Nieminen, *Journal of Applied Physics* **2013**, *113*, 133510.

[33] M. Malitckaya, H.-P. Komsa, V. Havu, M. J. Puska, *Advanced Electronic Materials* **2017**, *3*, 1600353.

[34] D. Cahen, R. Noufi, *Solar Cells* **1991**, *30*, 53.

[35] D. W. McKee, D. Chatterji, *Carbon* **1975**, *13*, 381.

[36] L. Kronik, U. Rau, J.-F. Guillemoles, D. Braunger, H.-W. Schock, D. Cahen, *Thin Solid Films* **2000**, *361–362*, 353.

[37] T. Hölscher, T. Schneider, M. Maiberg, R. Scheer, *Progress in Photovoltaics: Research and Applications* **2018**, *26*, 934.

[38] H. Mönig, D. Lockhorn, N. Aghdassi, A. Timmer, C. A. Kaufmann, R. Caballero, H. Zacharias, H. Fuchs, *Adv. Mater. Interfaces* **2014**, *1*, 1300040.

[39] D. Shin, J. Kim, T. Gershon, R. Mankad, M. Hopstaken, S. Guha, B. T. Ahn, B. Shin, *Solar Energy Materials and Solar Cells* **2016**, *157*, 695.

[40] J. Lehmann, S. Lehmann, I. Lauermann, T. Rissom, C. A. Kaufmann, M. Ch. Lux-Steiner, M. Bär, S. Sadewasser, *Journal of Applied Physics* **2014**, *116*, 233502.

[41] O. Knacke, O. Kubaschewski, *Thermochemical Properties of Inorganic Substances*, Springer-Verlag, Verlag Stahleisen, Berlin, New York, Düsseldorf, **1991**.

[42] S. K. Sahoo, R. Kormath Madam Raghupathy, T. D. Kühne, H. Mirhosseini, *J. Phys. Chem. C* **2018**, *122*, 21202.

[43] D. Cahen, R. Noufi, *Journal of Physics and Chemistry of Solids* **1992**, *53*, 991.

[44] E. M. Lanzoni, T. Gallet, C. Spindler, O. Ramírez, C. K. Boumenou, S. Siebentritt, A. Redinger, *Nano Energy* **2021**, *88*, 106270.

[45] J. Lee, L. Chen, U. Obahiagbon, C. Thompson, W. N. Shafarman, R. W. Birkmire, in *2013 IEEE 39th Photovoltaic Specialists Conference (PVSC)*, **2013**, pp. 0398–0401.

[46] S. Siebentritt, E. Avancini, M. Bär, J. Bombsch, E. Bourgeois, S. Buecheler, R. Carron, C. Castro, S. Duguay, R. Félix, E. Handick, D. Hariskos, V. Havu, P. Jackson, H.-P. Komsa, T. Kunze, M. Malitckaya, R. Menozzi, M. Nesladek, N. Nicoara, M. Puska, M. Raghuwanshi, P. Pareige, S. Sadewasser, G. Sozzi, A. N. Tiwari, S. Ueda, A. Vilalta-Clemente, T. P. Weiss, F. Werner, R. G. Wilks, W. Witte, M. H. Wolter, *Advanced Energy Materials* **2020**, *10*, 1903752.

[47] S. Béchu, A. Loubat, M. Bouttemy, M. Balestrieri, S. Gaiaschi, T. Hildebrandt, V. Archard, M. Frégnaux, D. Aureau, J. Vigneron, F. Donsanti, M. Jubault, P. Chapon, D. Lincot, J.-F. Guillemoles, A. Etcheberry, Waikoloa, **2018**.

[48] N. Nicoara, T. Lepetit, L. Arzel, S. Harel, N. Barreau, S. Sadewasser, *Scientific Reports* **2017**, *7*, 41361.

[49] S. A. Jensen, S. Glynn, A. Kanevce, P. Dippo, J. V. Li, D. H. Levi, D. Kuciauskas, *Journal of Applied Physics* **2016**, *120*, 063106.

The table of contents entry should be 50−60 words long, and the first phrase should be bold.

The surface and grain boundaries of sodium-doped CuInSe$_2$ thin film solar cell absorbers undertake reversible oxidation, unlike undoped films. The topographical features of the films observed by electron (SEM), He-ion (HIM) and Kelvin probe force (KPFM) microscopies are cross-correlated by cathodoluminescence spectroscopy (CL), secondary-ion mass spectrometry (SIMS) and contact potential difference (CPD) imaging, before and after long time under vacuum.

Keywords: PV, CIGS, alkali metal PDT, grain boundaries, electrostatic potential fluctuations

Finn Babbe, Nicoleta Nicoara, Harvey Guthrey, Nathalie Valle, Omar Ramirez Sanchez, Damien Aureau, Hossam Elanzeery, Deepanjan Sharma, José Luís Virtuoso, Jean-Nicolas Audinot, Anastasiya Zelenina, Sevan Gharabeiki, Tom Wirtz, Susanne Siebentritt, Phillip J. Dale, Sascha Sadewasser, Diego Colombara*

Vacuum-healing of grain boundaries in sodium-doped CuInSe$_2$ solar cell absorbers

ToC figure ((Please choose one size: 55 mm broad × 50 mm high **or** 110 mm broad × 20 mm high. Please do not use any other dimensions))

WILEY-VCH
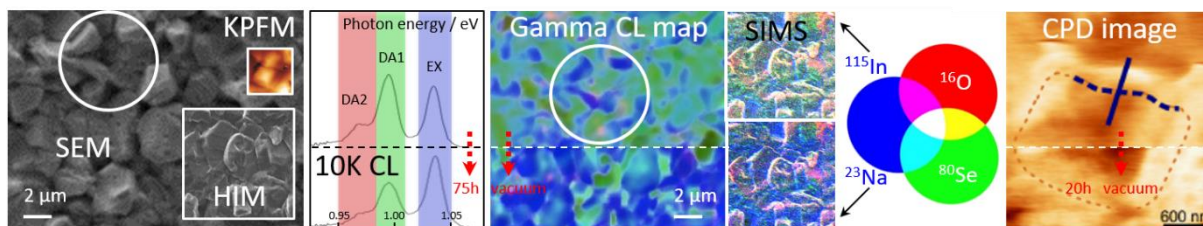
Supporting Information

Vacuum-healing of grain boundaries in sodium-doped CuInSe$_2$ solar cell absorbers

Finn Babbe, Nicoleta Nicoara, Harvey Guthrey, Nathalie Valle, Omar Ramirez Sanchez, Damien Aureau, Hossam Elanzeery, Deepanjan Sharma, José Luís Virtuoso, Jean-Nicolas Audinot, Anastasiya Zelenina, Sevan Gharabeiki, Tom Wirtz, Susanne Siebentritt, Phillip J. Dale, Sascha Sadewasser, Diego Colombara*

SIMS map data analysis

The Nano-SIMS images shown in Fig. 3a corresponding to the Na-doped CIS film before and after 96 h of UHV were processed to obtain (i) the percentage of correlation between the ^{16}O and (^{16}O^{23}Na) atomic cluster signals and (ii) the two-dimensional Fourier transform (2D-FFT correlation) typically used to detect similarities between two 2D signals expressed as matrices, according to Eq. 1. The results are shown in Fig. S1.

Eq. 1 $\quad r(\mathrm{i},\mathrm{j}) = \sum_{m=1}^{M} \sum_{n=1}^{N} a(m,n)b(m-i, n-j)$
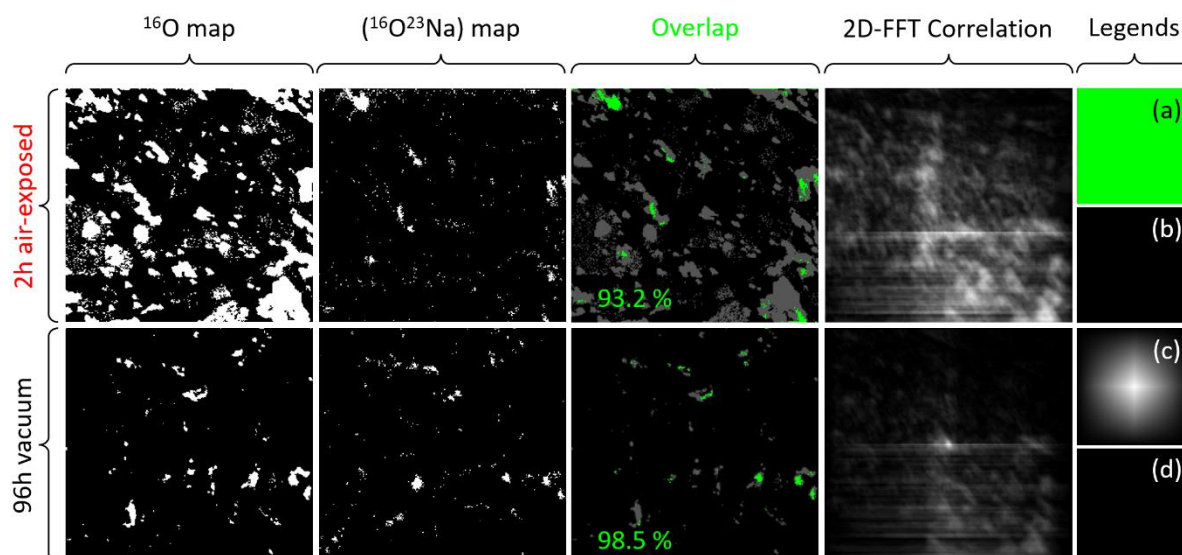
Fig. S1 ^{16}O and (^{16}O^{23}Na) Nano-SIMS images before (top row) and after vacuum (bottom row) expressed as binaries, along with the corresponding overlap and 2D-FFT correlation images. The legend is as follows. **(a-b)** Overlap analysis: overlapping areas are shown in green, while the regions of no signal are shown in black. The percentage numbers represent the portion of the overlapping area between the ^{16}O map and (^{16}O^{23}Na) atomic cluster map (shown as green area) that falls on regions where the ^{16}O signal is detected in the ^{16}O map. **(c-d)** 2D-FFT correlation: (c) corresponds to perfect correlation, while (d) corresponds to no correlation.

Assessment of O absorption/desorption cyclability by XPS
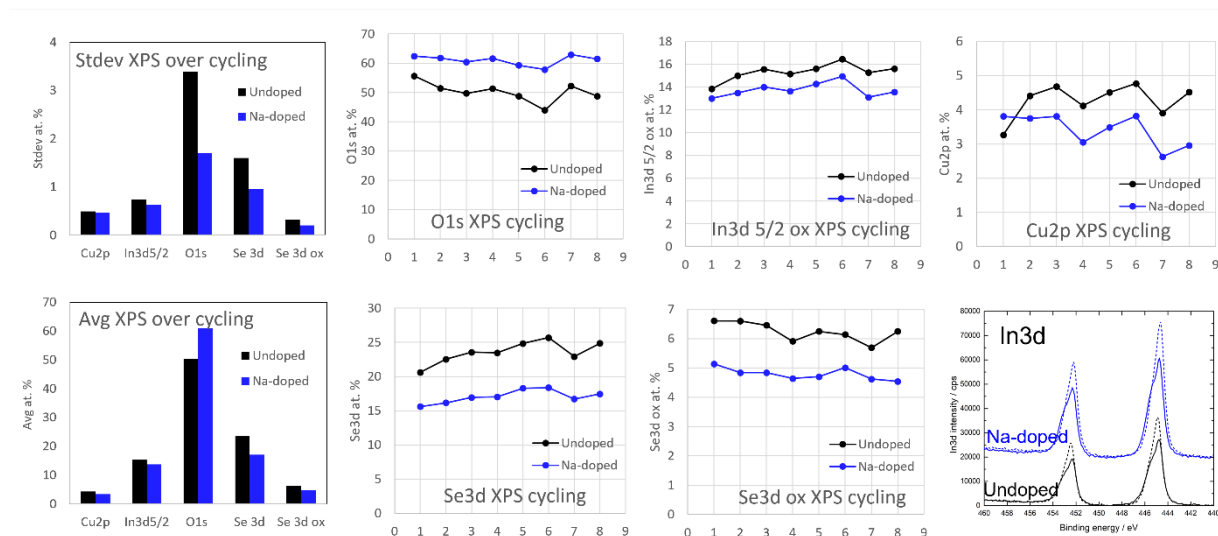
Fig. S2 XPS analysis. Average elemental concentration and variation over the following consecutive programme: (1) as-received; (2) after 18 h of vacuum; (3) after 12 h of vacuum; (4) after 1 h of air exposure; (5) after 18 h of vacuum; (6) after 88 h of vacuum; (7) after 48 h of air exposure; (8) after 18 h of vacuum, performed on undoped (black) and Na-doped CIS films (blue) that were not intentionally exposed to air before the experiment. The samples analysed for this experiment were aged in air under dark conditions for approximately 3 years. Offset In3d XPS spectra of undoped (black) and Na-doped (blue) CIS films after 2h of air exposure (solid lines) and subsequent 16h of vacuum (dashed lines).

XPS survey spectra and Na 1s high-resolution spectra
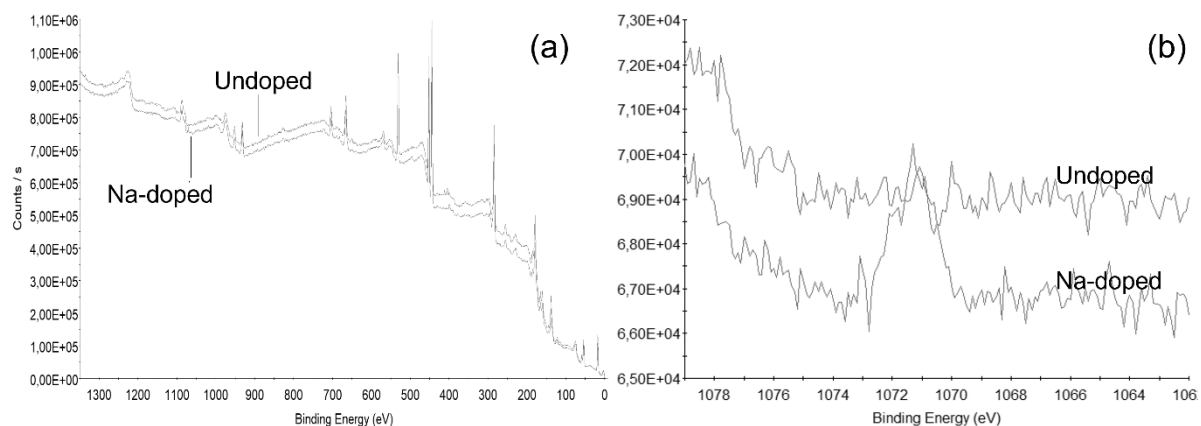
Fig. S3 XPS analysis. Survey spectra (a) and high-resolution spectra (b) of undoped and Na-doped $CuInSe_2$ films after KCN etching. The Na 1s peak is slightly detectable at 1071 eV.

Cathodoluminescence analysis

The maps shown in Fig. 4c were obtained by extracting gamma at each pixel over the scanned regions to visualize the spatial distribution of potential fluctuations with respect to the film microstructure. The gamma parameter was obtained from a fit to the low-energy portion of emission spectra based on Eq. 2 [49].

Eq. 2 $\quad I(h\nu) \propto \frac{1}{\gamma} e^{\left[\frac{(E_g - E_I - h\nu)^2}{2\gamma^2}\right]}$

where E_I is the acceptor ionization energy and γ is the magnitude of the potential fluctuations.
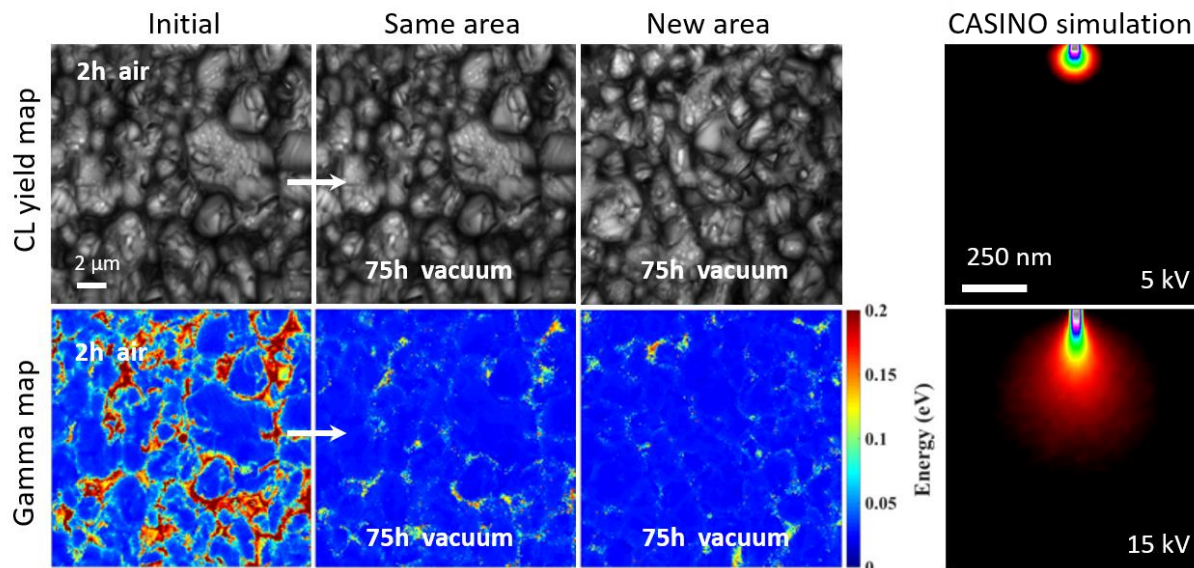
Fig. S4 CL yield (top) and gamma energy (bottom) map acquired at 300 K on the Na-doped CIS film after 2 h of air-exposure (initial) and after 75 h of vacuum in the SEM chamber acquired at same location and on a new area not exposed to the electron beam. Casino simulations of the CIS-electron beam interaction at 5 kV and 15 kV [31]: 80 % of the energy loss occurs within *ca.* 100 nm and *ca.* 200 nm from the film surface, respectively.